THE JOURNAL OF PHYSICAL CHEMISTRY B

Article

Cite This: J. Phys. Chem. B 2018, 122, 240−249

pubs.acs.org/JPCB

Charging and Transport Dynamics of a Flow-Through Electrode Capacitive Deionization System

Yatian Qu,[†,‡] Patrick G. Campbell,[‡] Ali Hemmatifar,[†] Jennifer M. Knipe,[‡] Colin K. Loeb,[‡] John J. Reidy,[§] Mckenzie A. Hubert,[∥] Michael Stadermann,*[,‡] and Juan G. Santiago*[,†]

[†]Department of Mechanical Engineering, Stanford University, Stanford, California 94305, United States

[‡]Lawrence Livermore National Laboratory, 7000 East Avenue, Livermore, California, United States

[§]Department of Chemistry, Stanford University, Stanford, California 94305, United States

[∥]Department of Chemical Engineering, Stanford University, Stanford, California 94305, United States

Supporting Information

ABSTRACT: We present a study of the interplay among electric charging rate, capacitance, salt removal, and mass transport in "flow-through electrode" capacitive deionization (CDI) systems. We develop two models describing coupled transport and electro-adsorption/desorption which capture salt removal dynamics. The first model is a simplified, unsteady zero-dimensional volume-averaged model which identifies dimensionless parameters and figures of merits associated with cell performance. The second model is a higher fidelity area-averaged model which captures both spatial and temporal responses of charging. We further conducted an experimental study of these dynamics and considered two salt transport regimes: (1) advection-limited regime and (2) dispersion-limited regime. We use these data to validate models. The study shows that, in the advection-limited regime, differential charge efficiency determines the salt adsorption at the early stage of the deionization process. Subsequently, charging transitions to a quasi-steady state where salt removal rate is proportional to applied current scaled by the inlet flow rate. In the dispersion-dominated regime, differential charge efficiency, cell volume, and diffusion rates govern adsorption dynamics and flow rate has little effect. In both regimes, the interplay among mass transport rate, differential charge efficiency, cell capacitance, and (electric) charging current governs salt removal in flow-through electrode CDI.

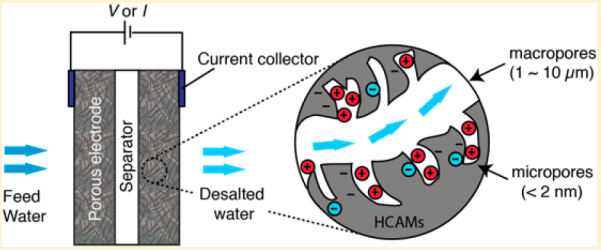

INTRODUCTION

Capacitive deionization (CDI) is an emerging technique for water desalination. CDI is especially promising for treating water with low and moderate salt concentration, also known as brackish water.[1,2] CDI operates at room temperature, low voltage (<1.2 V), and ambient pressure. It requires little infrastructure and thus scales favorably to various applications including portable fresh water suppliers and municipal desalination plants. The key component of a CDI cell is at least one pair of porous electrodes. Salt ions are removed from water and held electrostatically at pore surfaces. CDI cells operate in charge and discharge cycles. Upon application of charging voltage or current, salt ions are transported and trapped within electrical double layers (EDLs) inside pores through electroadsorption. The cell is then typically regenerated by discharging at zero voltage (or reversed bias)[2,3] or at a constant current to release adsorbed ions.

The operations of CDI systems always require flow. Flow can be introduced intermittently between charging and discharging steps to generate desalted water and brine in batches. Most commonly, flow is maintained in the entire operation cycle as a steady water stream. The coupling of charging and mass transport determines the dynamics of the deionization process, such as effluent salinity and water recovery ratio. It is thus vital to understand and characterize the interplay between charging rate and mass transport for optimal performance.

The coupling between charging and transport dynamics in a CDI cell is largely determined by its configuration. The most common CDI configuration is the "flow-between" architecture where the salt solution flows through a space between two porous electrodes.[4−8] There has been a few reported studies of the interplay among charging time scales, mass transport, and cell capacity for flow-between CDI. Zhao et al. showed that, with constant current (CC) charging, the effluent salt concentration of a membrane CDI (MCDI) cell can be tuned to a desired set point by adjusting flow rate and charging current.[4] Biesheuvel et al. presented a dynamic adsorption/desorption process model based on the Gouy−Chapman−Stern EDLs structure to predict time-dependent effluent concentrations of CDI experiments. Their model includes continuous flow but only demonstrates results of constant voltage (CV) charging and discharging.[9] Jande et al. developed a transient adsorption

Received: September 14, 2017
Revised: November 14, 2017
Published: January 2, 2018

DOI: 10.1021/acs.jpcb.7b09168
J. Phys. Chem. B 2018, 122, 240−249

mathematical model to predict effluent concentration minima and charging time in CDI (in CV mode) using charging and flow parameters, such as applied potential, flow rate, and electrode capacity.[10] In a subsequent study, Jande et al. presented a dynamic response model to describe the variation of the effluent concentration with time under CC charging.[11] However, none of these efforts have focused on identifying the governing nondimensional parameters around charging time versus flow rate, and there are no clearly identified figures of merit and nondimensional parameters governing this interplay.

The flow-between CDI architecture exhibits transport limitations. Although easier to assemble and seal, this traditional architecture is significantly limited by spacer-to-electrode diffusion times and inability to utilize the full adsorption capability of porous electrodes.[12] In the current study, we focus primarily on an alternative "flow-through electrode" architecture wherein fluid flow is driven directly through electrodes and the gap between electrodes is minimized.[12−14] We have referred to these cells as flow-through CDI in past publications but here introduce "flow-through electrode" CDI (fteCDI) to be more descriptive and distinguish our approach from previous uses of "flow-through CDI".[15,16] fteCDI electrodes enable fast ion transport through pores and full accessibility of the EDL capacitance of cell.[12] The interplay between charging dynamics and feedwater flow rate is especially important for fteCDI, since advection plays a major role in ion transport to adsorption sites within the porous electrode volume.

To our knowledge, the only studies that include system dynamics of fteCDI system are the work by Suss et al and by Guyes et al.[12,17] Suss et al. analyzed fteCDI operation in batch mode and with intermittent flow applied only during open (external) circuit phase between charging and discharging steps.[12] This batch mode may be easier to rationalize but likely limits throughput and fresh water production rate. Guyes et al. published a simple, one-dimensional fteCDI model which operates in CV charging mode. However, their study focuses on model-to-data agreement and includes little discussion on charging and transport dynamics in fteCDI systems.

Here, we focus primarily on understanding and characterizing the figures of merits associated in the interplay among charging time scales, mass transport, and cell capacity, particularly in fteCDI. We present two models to describe the desalination performance of an fteCDI system with a focus on understanding and characterizing the coupling effects of charging and mass transport for a given cell capacity. We primarily focus our study on CC mode as CC operation is more energy efficient than CV.[14] In addition, we mainly focus on CDI operation with single-pass continuous flow. We first present perhaps the simplest model which nevertheless captures essential dynamics: an unsteady zero-dimensional volume-averaged model. We use this simple model to identify nondimensional parameters and figures of merit associated with fteCDI temporal responses. We then present an area-averaged model based on area-averaged one-dimensional unsteady transport equations. This area-averaged model is based on a modified Donnan approach for capacitive ion charge storage,[18−21] and we consider a form applicable to capacitive deionization in porous electrodes including the effect of (immobile) native surface charge.[22−24] This second model captures both temporal fluctuations and variability along the direction of flow in an fteCDI cell. We validate modeling results by performing experiments with an fteCDI cell fabricated using hierarchical carbon aerogel monoliths (HCAMs) electrodes,[12,14,25,26] as shown in Figure 1a. We use both models to identify two

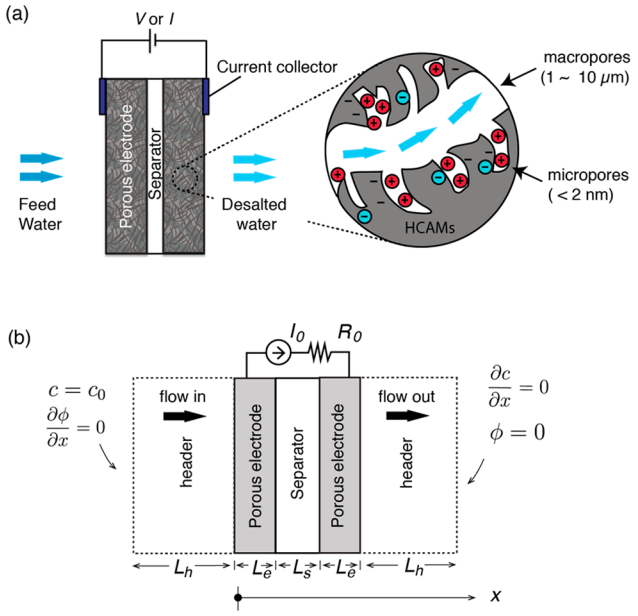

Figure 1. (a) Schematic of the flow-through electrodes CDI cell used in this study and the charging process inside porous electrode. The cell consists of a pair of 300 μm thick hierarchical carbon aerogel monolith (HCAM) electrodes, a 100 μm porous dielectric separator, two metal current collectors, and wires. The HCAM electrodes have a bimodal pore structure consisting of macropores (pore diameter ~1−10 μm) and micropores (pore diameter <2 nm). During the charging process, mobile ions from water (represented in red color) transported through macropores are electrostatically absorbed in micropores to compensate electrical charge (represented by negative sign) in carbon matrix. The carbon electrode surface also has immobile native charge (represented by blue ions) either introduced by surface group modification or electrochemical oxidation during operation. (b) Schematic of modeling domains and boundary conditions in one-dimensional area-averaged model. The length of separator is exaggerated for illustration (not reflecting the actual length used in simulations). For merely computation purpose, we include two artificial headers. The front header is to accommodate salt flux from upstream tubing and the rear header is needed for simulating concentration effluent properly.

important salt transport regimes and pose nondimensional parameters applicable to describe and quantify these regimes. To the best of our knowledge, our work is the first study centered on and characterize the interplay of charging and mass transport in CDI systems. Although we concentrate on fteCDI, we will briefly discuss differences between fteCDI, flow-between CDI and membrane CDI in terms of charging and flow interplay. Moreover, our models and analysis approach are potentially applicable to other electrochemical systems that involve charging and mass transport, such as flow batteries and fuel cells.

THEORY

Model I: Unsteady Zero-Dimensional Volume-Averaged Model. *Governing Transport Equation.* We here present an unsteady zero-dimensional volume-averaged model based on classical macroscopic porous electrode (MPE) theory[27−29] and a Gouy−Chapman−Stern (GCS) treatment of charge layers[9,30,31] to predict time-dependent effluent concentration c_e and identify performance metrics of an fteCDI cell. We start with the general form of MPE transport equation

$$p_M \frac{\partial}{\partial t}(c_i) + \nabla \cdot \mathbf{N}_i = a j_{in} \quad (1)$$

DOI: 10.1021/acs.jpcb.7b09168
J. Phys. Chem. B 2018, 122, 240−249

Here c_i is the concentration of ion species i in the pores. p_M is the porosity associated with macropores (the volume fraction of the pores contributing to mass transport pathways). $\mathbf{N}_i$ is the average molar flux vector in liquid phase, including contributions from advection, dispersion, and electromigration. Here, dispersion includes diffusion and mechanical spreading of ion species. j_{in} is the average molar flux across the interfacial area between the electrode matrix and liquid phase. a is the specific interfacial area, defined as the surface area of the porous electrode per unit volume of the total electrode.

We formulate transport equations within the porous electrode assuming bimodal pore structures and implement the GCS model to describe the EDLs formation. We assume the electrode materials possess larger transport pathways consisting of continuous micron-scale pore networks (which are typically termed "macropores" and have order >50 nm pore diameters) and smaller nanoscale pores (which are termed "micropores" and have order <2 nm pore diameters) as salt adsorption and desorption sources. We note that for HCAM materials, the primary transport pores have diameters greater than about 1 μm.[25] The GCS model assumes two nanoscopic charge layers: the diffuse layer in which the ions are nonspecifically electroadsorbed within the double layer and a compact layer of specifically absorbed molecules which separates the diffuse layer from the electrode surface. We use $\Delta\phi_{diff}$ to represent the voltage difference over the diffuse part of the double layer.

To develop this model, we will consider an averaging of the transport equations along a cross-sectional area normal to the primary flow direction through electrodes. This area averaging results in a one-dimensional geometry along the superficial flow direction (along direction x in Figure 1a) and introduces the effect of EDL electrostatic adsorption into the equations as a local sink/source term for ions. We assume uniform porosity throughout the electrodes and a binary, symmetric, univalent, and dilute electrolyte. The mass transport of ion species in macropores is thus formulated as

$$p_M \frac{\partial c}{\partial t} + u_{sup}\frac{\partial c}{\partial x} - p_M D_{BF}\frac{\partial^2 c}{\partial x^2} = -p_m \frac{\partial(a\Gamma)}{\partial t} \quad (2)$$

Here c is the ion concentration (local anion or cation concentration) in the electroneutral macropores. More details around the derivation of eq 2 are given in the Supporting Information (SI). Note the electroneutrality assumption applied within macropores implies that advection and diffusion are the only transport mode of the scalar quantity $(c_+ + c_-)$ (which we will hereafter refer to as "salt concentration").[32] In the volume averaging of salt concentration c, the characteristic length scale is considerably larger than macropore topological features but small enough to capture spatiotemporal variation. p_M is the porosity associated with macropores (the volume fraction of the pores contributing to mass transport pathways), and p_m is the porosity associated with micropores (the volume fraction of pores contributing to ion adsorption). u_{sup} is the superficial velocity, a hypothetical flow velocity calculated as the actual volume flow rate divided by the macroscopic cross-sectional area. Here D_{BF} is the one-dimensional Burnett−Frind hydrodynamic dispersion coefficient which approximates the effects of longitudinal dispersion of ion species due to both mechanical spreading and molecular diffusion in porous media.[33,34] $D_{BF} = \alpha_L u_{sup} + D_{eff}$, where α_L is a longitudinal dispersivity parameter and D_{eff} is the effective molecular diffusivity corrected to account for tortuosity (equal to the molecular diffusivity divided by tortuosity). The right-hand side of eq 2 is a sink or source term from MPE theory for ion adsorption or desorption. This term links the local macropore ion transport to adsorption/desorption in micropores. a is the electrode surface area per unit volume of electrode matrix, and we assume a is a uniform number across the electrode. Γ is the salt adsorption in units of moles per electrode surface area. We also define the local charge density on the electrode surface (in unit of moles per area) as σ. The expressions of Γ and σ can be found in section S-2 in the SI. A complete list of variables, parameters, and constants used in the volume-averaged model is presented in Table 1.

Table 1. Model Variables and Parameters

1.1 variables and parameters used in volume-averaged model

variable	description	units
c_e	effluent salt concentration	mM
Q	flow rate	mL/min
I_0	charging current	mA

parameter	description	value	units
c_0	feed salt concentration	50	mM
p_M	macropore porosity	0.57	
A_m	across-section area of electrode and separator	22.4	cm^2
L_e	thickness of electrode	300	μm
L_s	thickness of separator	100	μm
L	cell length, $L = 2L_e + L_s$	700	μm
V_0	entire cell volume, $V_0 = (2L_e + L_s)\,A_m$	1.57	cm^3
α_L	longitudinal dispersivity	10^{-4}	m
D_{eff}	effective molecular diffusion coefficient	6.65×10^{-10}	m^2/s
D_{BF}	Burnett-Frind hydrodynamic dispersion coefficient in electrodes	2.54×10^{-9}	m^2/s

1.2 variables and parameters used in area-averaged model[a]

variable	description	units
c	local salt concentration	mM
q	net charge density in micropore	mM
q_e	electronic charge density in the electrode matrix	mM
w	volumetric salt concentration in micropores	mM
ϕ	potential of local macropore liquid phase	V
ϕ_e	potential of electrode solid phase	V
$\Delta\phi_D$	Donnan potential	V
$\Delta\phi_m$	micropore potential drop	V

parameter	description	value	units
p_m	micropore porosity	0.1	
C_m	effective volume-specific capacitance of micropores	120	F/cm^3
q_{native}	immobile native charge density	100	mol/m^3
τ	tortuosity of electrodes	2.4	
R_c	contact resistance	1.1	Ω
$D_{BF,s}$	Burnett−Frind hydrodynamic dispersion coefficient in separator	2.54×10^{-9}	m^2/s

[a]We list here only the additional parameters which are not already included in volume-averaged model list of Table 1.1.

Next, we here define a local differential charge efficiency λ, the local ratio of salt adsorption/desorption per unit of net electrical charge transferred ($\lambda = (d\Gamma/d\sigma)$). λ links electrical charge in carbon matrix and salt adsorption in the pores.[9] In the GCS model, differential charge efficiency relates to diffuse layer potential $\Delta\phi_{diff}$ as $\lambda = \tanh(|\Delta\phi_{diff}|/(2V_T))$ where V_T is thermal voltage ($V_T = kT/e$, k and T being Boltzmann constant and temperature).[9] We replace salt adsorption/desorption rate $\partial(a\Gamma)/\partial t$ by $\lambda\partial(a\sigma)/\partial t$. The transport equation becomes

DOI: 10.1021/acs.jpcb.7b09168
J. Phys. Chem. B 2018, 122, 240−249

$$p_M \frac{\partial c}{\partial t} + u_{sup} \frac{\partial c}{\partial x} - p_M D_{BF} \frac{\partial^2 c}{\partial x^2} = -p_m \lambda \frac{\partial (a\sigma)}{\partial t} \quad (3)$$

Equation 3 is the governing equation for our volume-averaged model. We will later normalize this equation to identify salt transport regimes and simplify this equation to develop the unsteady zero-dimensional volume-averaged model.

Lumped Differential Charge Efficiency Formulation. To complete the volume-averaged model, we here develop a lumped differential charge efficiency. In the classical GCS model, the concentration of ion i in the diffuse layer follows a Boltzman distribution

$$c_i = c_\infty \exp\left(-\frac{z_i \phi}{V_T}\right) \quad (4)$$

where c_∞ is the ion concentration in bulk solution (or in macropore in our bimodal pore structures) and ϕ is the potential within the diffuse double layer relative to the local solution outside the double layer. z_i is the ion valence. In our volume-averaged model, we will assume the macropore concentration c_∞ is approximately the feed concentration c_0. Here we will make a typically Donnan type model assumption[4,5,18−20,22,35] where we assume that the potential and ion concentration c_i within micropores is a single uniform value. The potential difference between the carbon and this uniform value is $\Delta\phi_{diff}$. The ion concentrations within the micropore are then

$$c_+ = c_0 \exp\left(-\frac{\Delta\phi_{diff}}{V_T}\right), \quad c_- = c_0 \exp\left(\frac{\Delta\phi_{diff}}{V_T}\right) \quad (5)$$

Hence, the total ion accumulation of net ionic charge within an electrode of macroscopic volume V_e (equal to $\pm I_0 t$ in CC charging) is then

$$\pm I_0 t = \mp p_m V_e F (c_+ - c_-) = \mp p_m V_e F c_0 \left[\exp\left(-\frac{\Delta\phi_{diff}}{V_T}\right) - \exp\left(\frac{\Delta\phi_{diff}}{V_T}\right)\right] \quad (6)$$

We can now consider a lumped form of charge efficiency λ that is applicable to the entire cell. To this end, we identify and explore two regimes for λ: (1) $\lambda < 1$ and (2) $\lambda = 1$. These regimes are respectively early/low voltage phase and longer-term/significant voltage phase.

We first describe the early phase of charging. In this phase, we assume the argument of the hyperbolic tangent is smaller than unity so we approximate $\tanh(|\Delta\phi_{diff}|/(2V_T))$ as $|\Delta\phi_{diff}|/(2V_T)$. Further, within the range of $0 \le (\Delta\phi_{diff}/V_T) \le 2$, we linearize $\exp(\Delta\phi_{diff}/V_T)$ and $\exp(-\Delta\phi_{diff}/V_T)$ in eq 6 as $1 + 2(\Delta\phi_{diff}/V_T)$ and $1 - 2(\Delta\phi_{diff}/V_T)$, respectively

$$\pm I_0 t = \mp p_m V_e F c_0 \left[\left(1 - 2\frac{\Delta\phi_{diff}}{V_T}\right) - \left(1 + 2\frac{\Delta\phi_{diff}}{V_T}\right)\right] = \pm 4 p_m V_e F c_0 \frac{\Delta\phi_{diff}}{V_T}. \quad (7)$$

We then arrive at an approximation of $\Delta\phi_{diff}$ using c_0, p_m, charging current I_0, and electrode volume V_e as

$$\Delta\phi_{diff} = \frac{I_0 t}{4 p_m V_e c_0 F} \quad (8)$$

Substituting eq 7 into the approximate form λ, we obtain the lumped differential charge efficiency λ for early charging as

$$\lambda \approx \frac{|\Delta\phi_{diff}|}{2V_T} \approx \frac{I_0 t}{8 p_m V_e c_0 F^2} \quad (9)$$

At longer charging times (and potentials $\Delta\phi_{diff}$ greater about twice the thermal voltage), the differential charge efficiency approaches unity, $\lambda = 1$. From eq 9, the characteristic time scale for lumped differential charging efficiency reaching unity is $t_\lambda = 8 p_M V_e c_0 F / I_0$. We will later use the lumped differential charge efficiency λ in two regimes ($\lambda < 1$ and $\lambda = 1$) to relate salt removal and electrical charge accumulation in volume-averaged model.

Identification of Transport Regimes. We now identify salt transport regimes by revisiting the governing transport equation (eq 3) and performing normalization. In eq 3, concentration c is nondimensionalized by feed concentration c_0 as $c^* = c/c_0$, and time t is normalized by the characteristic time scale of charge efficiency $t^* = t/t_\lambda$, and local charge density change rate $\frac{\partial(a\sigma)}{\partial t}$ (in unit of moles per electrode volume) is normalized by globally average volumetric salt adsorption rate $I_0/(V_0 F)$. The dimensionless form of eq 3 is

$$\frac{L}{u_{sup} t_\lambda} \frac{\partial c^*}{\partial t^*} + \frac{1}{p_M} \frac{\partial c^*}{\partial x^*} - \frac{D_{BF}}{u_{sup} L} \frac{\partial^2 c^*}{\partial x^{*2}} = -\frac{p_m I_0 L \lambda}{p_M t_\lambda V_0 F c_0 u_{sup}} \frac{\partial (a\sigma)^*}{\partial t^*} \quad (10)$$

We define a dimensionless Peclet-type number as $Pe^* = \frac{u_{sup} L}{p_M D_{BF}}$ to compare the contributions of advection and dispersion (not just molecular diffusion) in mass transport. Depending on the value of Pe^*, we perform our theoretical analysis and experiments of fteCDI performance in two transport regimes: (1) advection-limited ($Pe^* \gg 1$) and (2) dispersion-limited ($Pe^* < 1$) regimes. In regime (1), we can safely neglect the dispersion term in eq 3 as it is much smaller than the advection term. In a similar manner, we can neglect the advection term in regime (2). We note that a second dimensionless number can be drawn from eq 10. Strouhal number can be defined as $St^* = \frac{L}{u_{sup} t_\lambda}$ to compare advection time scale to charge sourcing time scale. Strouhal number is useful for identifying regimes of charging states. However, for this work, we focus on transport regimes characterized by Peclet-type number Pe^*, and the analysis using Strouhal number will be included in future work.

Unsteady Zero-Dimensional Volume-Averaged Model. We now derive a lumped version of governing transport equation (eq 3) to arrive at an unsteady zero-dimensional volume-averaged model. In this derivation, we focus on the advection-limited regime ($Pe^* \gg 1$) since it is the most interesting regime for fteCDI. To simplify eq 3 to zero-dimensional, we perform volume integration of eq 3 across the entire fteCDI cell. To do this, we assume a uniform differential charge efficiency across the entire electrode and define a cell average concentration as $p_M V_0 \frac{\partial \bar{c}}{\partial t} \approx \int p_M \frac{\partial c}{\partial t} \, dV$. We also approximate the cell average concentration $\bar{c}$ as half of the sum of inlet and outlet concentrations $\frac{1}{2}(c_0 + c_e)$. We note that this approximation implies an assumption of linear concentration profile inside the cell, which is only valid when advective transport of ions balances electrostatic adsorption. Therefore, the derived equations of volume-averaged model only apply to advection-limited regime.

DOI: 10.1021/acs.jpcb.7b09168
J. Phys. Chem. B 2018, 122, 240−249

We then apply divergence theorem and approximate the inlet and outlet boundary conditions as $\frac{\partial c}{\partial x} = \frac{c_e - c_0}{2L_e + L_s}$ at $x = 0$ and at $x = 2L_e + L_s$. We arrive at a zero-dimensional (in space) ordinary differential equation (ODE) for c_e, as shown in eq 11. Further details of this derivation are included in the SI.

$$\frac{\partial c_e}{\partial t} + \frac{2Q}{p_M V_0}(c_e - c_0) = -\frac{2\lambda I_0}{p_M V_0 F} \tag{11}$$

The terms on the left-hand side of this equation correspond to respectively the accumulation within the cell and the net transport due to advection and dispersion. The right-hand side is the sink/source term associated with electrostatic adsorption.

We now substitute the expression for lumped differential charge efficiency as derived in eq 9. We then express eq 11 for the two regimes of lumped charge efficiency ($\lambda < 1$ and $\lambda = 1$) as follows:

$$\begin{cases} \dfrac{\partial c_e}{\partial t} + \dfrac{2Q}{p_M V_0}(c_e - c_0) = -\dfrac{{I_0}^2}{4p_M p_m V_0 V_e c_0 F^2} t \ (\lambda < 1) \\ \dfrac{\partial c_e}{\partial t} + \dfrac{2Q}{p_M V_0}(c_e - c_0) = -\dfrac{2I_0}{p_M V_0 F} \ (\lambda = 1) \end{cases} \tag{12}$$

We analytically solve eqs 12. For the ODE in the regime of $\lambda < 1$, the solution is:

$$c_e(t) = c_0 - \left(\frac{B}{A^2}\right)(1 - e^{-At}) + \left(\frac{B}{A}\right)t, \quad \left(t < \frac{8p_M V_e c_0 F}{I_0}\right) \tag{13}$$

where

$$\begin{cases} A = \dfrac{2Q}{p_M V_0}, \\ B = -\dfrac{I_0^2}{4p_m p_M V_0 V_e c_0 F^2} \end{cases} \tag{14}$$

For ODE in the regime of $\lambda = 1$, the solution is then

$$c_e(t) = \left(\frac{C}{A}\right) + k_1(e^{-At}) + c_0, \quad \left(t \geq \frac{8p_M V_e c_0 F}{I_0}\right) \tag{15}$$

where

$$\begin{cases} A = \dfrac{2Q}{p_M V_0}, \\ C = -\dfrac{2I_0}{p_M V_0 F} \end{cases} \tag{16}$$

Here the parameter k_1 is determined by the initial condition which is c_e ($t = 8p_M V_e c_0 F/I_0$) from eq 13.

We present the detailed derivation of analytical solutions (eqs 13 and 15) in the SI. We will present predictions based on this model in the Results and Discussion. We caution that this volume-average model is not applicable to the dispersion limited regime ($Pe^* < 1$). Dispersion (and diffusion) limited cells experience a global "starvation" condition where advective transport is insufficient to replenish ions for electroadsorption, and the resulting strong ion depletion within the electrode strongly violates the assumption of linear concentration profile inside the cell and the assumption for lumped differential charge efficiency that the macropore concentration is constant and uniform at an approximate value of c_0.

Although simple, this volume-averaged model clearly identifies a characteristic time scale for charging efficiency as $t_\lambda = 8p_M V_e c_0 F/I_0$, which is the characteristic time required for the charging process to approximately achieve a differential charge efficiency of unity. We will therefore normalize charging time as $\overline{t} = t/t_\lambda$ in both the volume-averaged and the area-averaged models. From this model, we also identify a characteristic quasi-steady-state condition wherein the advective influx of salt is balanced by a constant electroadsorption rate (with approximate charge efficiency of unit). We can derive this characteristic steady effluent concentration c_e under CC operation by setting ($\partial c_e/\partial t = 0$ and $\lambda = 1$ in eq 12

$$(c_e - c_0) = \frac{I_0}{FQ} \tag{17}$$

Hence, in both the volume-averaged model and in the area-averaged model we will normalize the effluent concentration as $\overline{(c_e - c_0)}/(I_0/(FQ))$.

Model II: Higher Fidelity Area-Averaged Model Using the Modified Donnan (mD) Model with Native Charge. In this section, we present a more comprehensive higher fidelity area-averaged model which captures both temporal fluctuations and variability along the flow direction of an fteCDI cell. We adopt the mD treatment of EDLs in bimodal pore structure electrodes. We include a formulation for immobile native charge in the micropores to account for nonelectrostatic adsorption.[22−24,36] We will use this model to both benchmark the simpler model of the previous section and further study charging dynamics. We will also compare both models with experimental results (see the Results and Discussion).

For the area-averaged model, we again consider a one-dimensional area-averaging approach and the similar assumptions regarding the electrolyte solution (binary, symmetric, univalent, and dilute) as the volume-averaged model. Figure 1b shows the modeling domains and boundary conditions in this area-averaged model.

The complete mass transport of ion species i in macropores is then

$$p_M \frac{\partial}{\partial t}(c_{M,i}) + \nabla \cdot \left[c_{M,i} u_{sup} - p_M D_{BF,i} \nabla c_{M,i} - \frac{p_M}{\tau} \mu_i c_{M,i} \nabla \phi\right] = -p_m \frac{\partial}{\partial t}(c_{m,i}) \tag{18}$$

where τ is the tortuosity of electrode material and ϕ is the potential of local macropore liquid phase. Other variables and parameters have the same definitions as those used in volume-averaged model. We again assume electroneutrality holds within macropores and thus $c = c_{M,i}$ for $i = \pm 1$. Again, we assume the same Burnett−Frind dispersion coefficient and the same mobility for both ion species, so that $D_{BF} = D_{BF,i}$ and $\mu = \pm\mu_i$ for $i = \pm 1$.

By adding and subtracting eq 18 for anions and cations, we derive the governing equations for mass transport of salt and charge balance in macropores as respectively

$$p_M \frac{\partial c}{\partial t} + u_{sup} \frac{\partial c}{\partial x} - p_M D_{BF} \frac{\partial^2 c}{\partial x^2} = -p_m \frac{\partial w}{\partial t} \tag{19}$$

DOI: 10.1021/acs.jpcb.7b09168
J. Phys. Chem. B 2018, 122, 240−249

$$\frac{p_M}{\tau}\mu\frac{\partial}{\partial x}\left(c\frac{\partial\phi}{\partial x}\right) = p_m\frac{\partial q}{\partial t} \quad (20)$$

Here w is half of the volumetric salt concentration in micropores, defined as $2w = c_m^+ + c_m^-$ where c_m^+ is cation concentration and c_m^- is anion concentration in micropores. q is the half of net charge density in micropore as q ($2q = c_m^+ - c_m^-$, with unit of moles per volume).

Considering charge balance in the electrode and electrolyte matrix, we have

$$2q + q_{native} + q_e = 0 \quad (21)$$

Here q_{native} is volumetric charge density of immobile native charge on electrode surface, in units of moles per volume. For carbon electrodes, the native charge may be introduced, for example, during the material synthesis process or during CDI operation by electrochemical oxidation of carbon.[6,16,37,38] q_e is the electronic charge density in the carbon.

Next, we relate electronic charge q_e to the micropore potential drop $\Delta\phi_m$ (potential difference between electrode surface and the center of micropore) as

$$\Delta\phi_m = q_e\frac{F}{C_m} \quad (22)$$

Here F is the Faraday constant. C_m is defined as the effective volume-specific capacitance of micropores, which we call micropore capacitance.[19] In addition, $\Delta\phi_m$ and Donnan potential $\Delta\phi_D$ are related to the potential difference between the electrode phase ϕ_e and the local macropore liquid phase ϕ as

$$\Delta\phi_m + \Delta\phi_D + \phi = \phi_e \quad (23)$$

Lastly, we close the system of equations by introducing a charge conservation relation between external constant current source I_0 and accumulative electronic charge q_e.

$$I_{ext} = I_0 = p_m\int\frac{\partial(q_eF)}{\partial t}\,dV \quad (24)$$

We note here that we have presented a set of equations which model transport and charging dynamics of fteCDI systems under CC operation. These equations can be modified to apply to CV operation, and we present the full CV formulation in the SI.

We performed parameter extraction to obtain the values of key fitting parameters in the model. The extraction process is discussed in the Results and Discussion. A summary of the variables and parameters used in the area-averaged model is listed in Table 1. All numerical simulations were performed with a commercially available finite element simulation software (COMSOL Multiphysics, 5.1, Burlington, U.S.A.).

EXPERIMENTAL METHODS

We performed experiments to study the coupling of charging and mass transport and to validate our fteCDI models. We also use these experiments to demonstrate the applicability of the dimensionless parameters identified by the volume-averaged model to scale and rationalize fteCDI dynamics. We particularly focus on the intimate interplay and competition among flow rate, charge accumulation rate, and charge efficiency.

Flow-Through Electrode CDI Cell. We fabricated a flow-through electrode CDI (fteCDI) cell to validate model predictions and study charging dynamics. The fteCDI cell was made of two blocks of hierarchical carbon aerogel monoliths (HCAMs) material[12,20,25,26] with an area of 4 × 6 cm and a thickness of 300 μm. The density of HCAM material is 0.53 g/cm^3 and each electrode weighs approximately 0.83 g. We used a 100 μm porous paper filter as a separator to insulate between the two electrodes. We used silver epoxy to create intimate electrical contacts between HCAM electrodes and copper wires.[13] The two porous electrodes and a separator were stacked into an assembly and glued on to a polycarbonate frame using epoxy. This assembly was then sandwiched between two 6 × 7.5 cm polycarbonate end plates with 400 μm silicone rubber sheets as gaskets. Both end plates were milled to accommodate two tubulations: one as a port to flow water, and the other one as a port to release trapped air. The cell was assembled using ten bolts. The cell assembly frame and housing parts were fabricated from polycarbonate.

Experiment Procedures. We performed continuous flow CDI experiments using our fteCDI cell with 50 mM NaCl. We adopted a CC charging scheme as our previous study shows CC charging mode is much more energy efficient than CV operation (for equal charge and time of charging).[14] As shown in the schematic of experimental setup in Figure 2, we used a

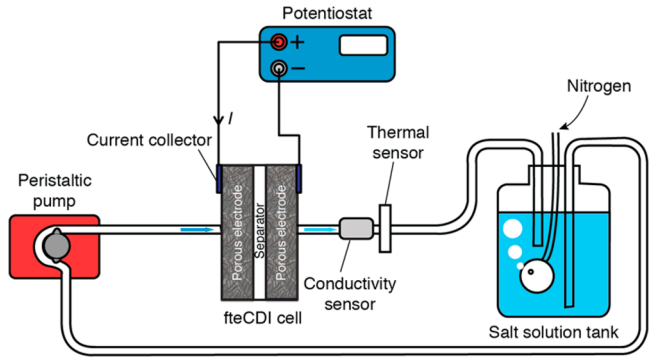

Figure 2. Schematic of experimental setup. We fabricated a flow-through electrode CDI cell with two blocks of hierarchical carbon aerogel monoliths material to perform charging experiments. We used a potentiostat to supply constant current at 50 mA and monitor electrical responses. A flow-through conductivity sensor was attached to the CDI cell downstream to measure the conductivity of effluent solution. A homemade flow-through thermal sensor was used to monitor the effluent solution temperature. We used a peristaltic pump to flow feed solution through the cell at various flow rates and with closed-loop circulation in a 50 mM NaCl solution tank. We continuously purged feed solution with house nitrogen to remove dissolved oxygen.

Biologic SP-300 potentiostat (Bio Logic Science Claix, France) to supply current and monitor electrical responses. A flow-through conductivity sensor (Edaq, Denistone East, Australia) was attached to the CDI cell downstream to measure the conductivity of effluent solution. A homemade flow-through thermal sensor was used to monitor the effluent solution temperature. We used a peristaltic pump (Watson Marlow 120U/DV, Falmouth, Cornwall, U.K.) to flow feed solution through the cell at various flow rates and with closed-loop circulation (flow from solution container to fteCDI cell and back to container). We continuously purged feed solution with house nitrogen to remove dissolved oxygen. Before experiments, we flowed sodium chloride solutions through the cell without charging for 30 min at 2.4 mL/min to allow the cell to equilibrate with solutions.

We first performed CC charging experiments at 50 mA with flow rates at 2.5, 5.1, 7.7, 10.3, and 12.8 mL/min to demonstrate

DOI: 10.1021/acs.jpcb.7b09168
J. Phys. Chem. B 2018, 122, 240−249

CDI charging and mass transport in advection limited regime. We calculate the dimensionless Peclet-type number Pe^* of fluid flow in this regime as 8.8 to 11. To rapidly regenerate the cell after charging (for convenience and expediency), we discharged the cell in CV mode at zero voltage. To operate the CDI cell in the dispersion limited regime, we charged the cell with 50 mA constant current at flow rates of 0.03, 0.10 and 0.22 mL/min, and followed by CV discharge. In this operational regime, Pe^* is smaller than or on the order of unity. For each experiment, we repeated charging and discharging cycles five times and used the data from last three cycles for model validation.

RESULTS AND DISCUSSION

Parameter Extraction. There is one fitting parameter in the (zero dimensional) volume-averaged model and an additional three fitting parameters used for the area-averaged model. These four parameters are respectively microporosity p_m, micropore capacitance C_m, native charge density q_{native} and longitudinal dispersivity α_L. We determined these values using preliminary experiments with the cell. For this parameter extraction, we fitted model predictions to the experimentally measured near-equilibrium salt adsorption and charge storage of our cell under CV operations (see section S-6 in the SI). We obtained the fitted values of C_m, q_{native}, and p_m and list these values in Table 1. We then fitted the experimental outlet effluent concentrations under CC operation mode to the CC area-averaged model to obtain values of dispersivity α_L, also shown in Table 1. We discuss further issues around this parameter extraction in the SI, and note here that three values of the fitted parameters are similar to those reported in literature for porous carbon materials (see for example Gao et al reported C_m as 135 F/cm^3 and immobile native charge as 200 mM;[24] Suss et al. reported C_m as 130 F/cm^3;[20] and Hemmatifar et al. have fitting values for C_m and p_m as 150 F/cm^3 and 0.3, respectively,[19]).

In Figure 3a we show results for the effluent salt concentration for the fteCDI as a function of time for both the volume-averaged and area-averaged models. The volume-averaged model captures many of the qualitative features of the area-averaged model. This includes an initial nearly linear drop in effluent concentration, and the subsequent approximate leveling off of the effluent concentration observed in the quasi-steady-state operation described earlier (wherein unity charge efficiency results in an approximately constant adsorption rate). The inlet-to-outlet reduction in effluent salt concentration in this quasi-steady operation is proportional to applied current divided by flow rate as suggested by the volume-averaged model (c.f. Equation 12). We see also that the volume-averaged model levels off at a time scale faster than the area-averaged model, which we attribute to the effect of nonuniform charging of the electrode predicted by the area-averaged model (see the SI for spatiotemporal plots of salt concentration predicted by the area-averaged model). We note that the key nondimensional parameters we derived here also provide insights for the scale-up of fteCDI systems. For example, eq 17 suggests that to maintain the same level of effluent salt removal, large flow rate desalination requires higher input electrical current.

Advection-Limited Regime. As we mentioned in the THEORY section, we divide our fteCDI cell operations and theoretical analysis into two distinct transport regimes: (1) advection-limited regime ($Pe^* \gg 1$) and (2) dispersion-limited regime ($Pe^* < 1$). fteCDI has unique operation regimes compared to other CDI architectures. Unlike traditional flow-between CDI whose desalination rate is primarily limited by the diffusion of ions from the separator to electrode pores,[12] fteCDI enables salt adsorption in the advection-limited regime and utilizes the full adsorption capability of porous electrodes. Therefore, the advection-limited regime is especially important for fteCDI cells, and we here emphasize this transport regime.

In the advection-limited regime, we study cell dynamics with flow rates ranging from 2.5 to 12.8 mL/min (respective values of Pe^* are between 8.8 and 11). From the volume-averaged model, we identified two dimensionless parameters associated with this regime. As described earlier, the proper characteristic time is a charge efficiency time scale, characterized by $t_\lambda = 8p_M V_e c_0 F/I_0$. Similarly, the scaling of effluent concentration in advection-limited operation should be the difference $(c_e - c_0)$ normalized by the quasi-steady (i.e., unity charge efficiency) electroadsorption rate $I_0/(FQ)$.

We first compare simulation results from the unsteady zero-dimensional volume-averaged model and the higher fidelity area-averaged model. For an fteCDI cell, the concentration of effluent streams evaluates its salt removal performance. In Figure 3a, the solid lines represent effluent concentration profiles predicted by the volume-averaged model. Dotted lines are simulation results from the area-averaged model. The volume-averaged model predicts a gradual reduction of effluent concentration at the early stage of charging, followed by an approximate leveling off at quasi-steady state. The distinct concentration

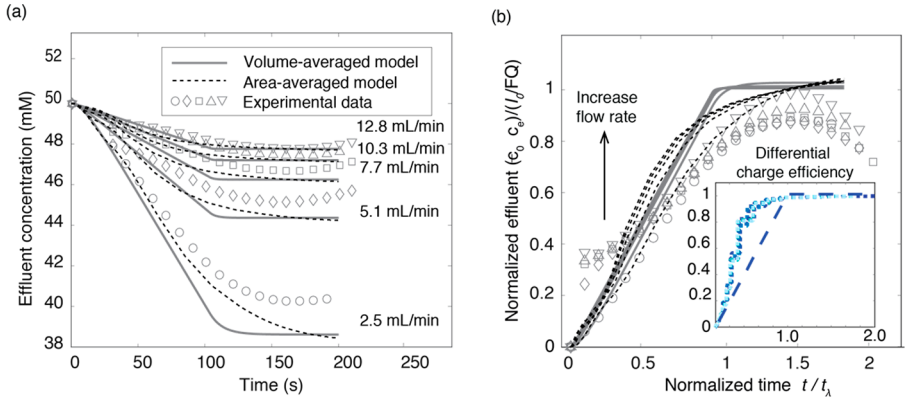

Figure 3. (a) Original and (b) normalized effluent concentration profiles from experiments (markers), volume-averaged model simulations (solid grayscale lines), and area averaged model simulations (short-dotted grayscale lines) in advection-limited regime, with single-pass continuous flow rates at 2.5, 5.1, 7.7, 10.3, and 12.8 mL/min. The fteCDI cell is operated in constant current charging mode at 50 mA.

DOI: 10.1021/acs.jpcb.7b09168
J. Phys. Chem. B 2018, 122, 240−249

profiles at early stage and at quasi-steady state corresponds to the two regimes of lumped differential charge efficiency: ($\lambda < 1$ and $\lambda = 1$). Simulation results from area-averaged model agree with predictions from the volume-averaged model but exhibit a smoother transition between the two differential charge efficiency regimes. The area-averaged model serves as an important benchmark for the volume-averaged model and validates the utility of the dimensionless parameters identified by the volume-averaged model. We attribute the discrepancy between volume-averaged model and area-averaged model to the effects of nonuniform charging and transport through the electrodes.

We now compare simulation results to experimental data. The markers in Figure 3a represent experimental results obtained in CC mode with 50 mA charging current. As predicted by simulations, in the early stage of the deionization process, salt adsorption is limited by differential charge efficiency irrespective of a steady and strong transport of salt into the cell via advective mass transport. At low applied potentials, the symmetry between enrichment and depletion of respectively counter-ions and coions within each electrode (c.f. eq 7) implies that early charging only "swaps" ions at electrode in micropores and little net ions, or salt, is trapped by the cell. As the cell charges, the nonlinearity of the Boltzmann distribution of trapped salt in the micropores results in a faster rate of increase in counterion versus coion concentration in micropores so new differential electrical charge efficiently traps salt proportionally and λ approaches unity. For $\lambda = 1$, a constant applied current I_o implies a constant electroadsorption rate. In this quasi-steady operation, the reduction in salt concentration scales by with the ratio I_0/Q. Comparing simulation results to experimental data, both the volume-averaged model and area-averaged model demonstrate fair agreement with trends and magnitudes of the experiments, suggesting that our models capture at least the qualitative dynamics. Models capture the qualitative shape of curves and approximate time scales and effluent concentration magnitudes of advection-limited fteCDI cell operation. One important discrepancy is the predicted constant salt concentration in the quasi-steady state. This is in contrast to the measurements which show an eventually early increase toward inlet concentration. This empirical behavior usually occurs around 150 s and when the cell voltage reaches 0.7 V (see section S-7 in the Supporting Information). We attribute this discrepancy between simulations and experiments to charge loss caused by parasitic reactions on electrodes.[16,39−41] Parasitic reactions provide current leakage paths, and therefore lower the differential charge efficiency for salt adsorption, and this charge loss mechanism is not captured in the current models. In addition, parasitic reactions dissipate power without trapping salt and practical operation of the cell should manage this power loss.[8]

These trends and limiting parameters suggest the normalization we show in Figure 3b. Here we leverage the scaling suggested by the volume-averaged model to normalize the predictions of both models as well as the experimental data. In the advection-limited regime, ion transport is sufficient to provide a steady supply of ions, and so charging current and differential charge efficiency are the limiting factors governing the effluent concentrations. Therefore, we normalize charging for advection-limited regimes by the characteristic time scale t_λ. When charging transition to the quasi-steady state, advective influx of salt is balanced by a constant electroadsorption rate (with approximate charge efficiency of unit). Hence, the appropriate normalization for effluent concentration is $\overline{(c_e - c_0)} = (c_e - c_0)/(I_0/(FQ))$, as suggested by eq 17. The inset in Figure 3b (the constant slope shown with a dashed line) plots the lumped differential charge efficiency, as discussed in the section Model I: Unsteady Zero-Dimensional Volume-Averaged Model.

Shown in Figure 3b are normalized effluent difference $\overline{(c_e - c_0)}$ versus normalized time $\overline{t} = t/t_\lambda$. First, the collapse of $\overline{(c_e - c_0)}$ vs $\overline{t}$ for the volume-averaged model curves is expected from the formulation. Second, we see that this scaling suggested by the volume-averaged model very well collapses the curves of the area-averaged model. These numerical predictions collapse into a tight group, with the exception perhaps of the numerical prediction for lowest flow rate where the area-averaged model exhibits the most nonuniform charging distributions. Third, and most importantly, we see that the scaling suggested by the volume-averaged model well collapses all of the experimental data into its own reasonably tight group. Further, we see the experimental data maximizes at about a value of unity, a result of near unity charge efficiencies observed for these data. We note that it seems that dimensionless time $\overline{t}$ can be approximated as $\overline{t} = t/t_\lambda \approx \lambda$ from eq 9 and the definition of t_λ. From the derivation of lumped differential charge efficiency λ (eq 9), λ is linearly proportional to time t before it approaches unity. Hence, it is not surprising that time t normalized by t_λ is directional proportional to λ. In other words, $\overline{t}$ demonstrates the evolution of differential charge efficiency λ in dimensionless time before λ reaches unity. However, when λ reaches unity in quasi-steady state, the approximation $\overline{t} = t/t_\lambda \approx \lambda$ is no longer valid.

We note that in advection-limited regime, the interplay of mass transport, differential charge efficiency, and charge accumulation rate determines the desalination performance of an fteCDI cell. The low differential charge efficiency at the early stage of electroadsorption process poses a limitation on salt removal and water recovery (the volume ratio of collected desalted water over feedwater). To overcome this challenge, we might charge and discharge the cell within a voltage window where the lowest potential is still above the voltage threshold to achieve unity differential charge efficiency.[42] We also note that, as reported in literature, membrane CDI do not demonstrate the current degree of low differential charge efficiency at the beginning of charging process, and this is because ion exchange membranes significantly enhance differential charge efficiency (at some expense of increased resistance and cost) and making it insensitive to EDL structure.[4,5,35,42]

Dispersion-Limited Regime. The area-averaged model allows us to explore regimes where dispersion (e.g., diffusion) fluxes are on the same order as or larger than advective fluxes. Hence, we chose flow rates of 0.03, 0.10, and 0.22 mL/min, corresponding to Pe^* of 0.2, 0.7, and 1.3, respectively. We note the lowest flow rate achievable was limited by the minimum repeatable flow rate of our peristaltic pump.

In the dispersion-limited regime, mass transport of ions is the major limiting factor. The cell is globally "starved", decoupling adsorption rate from applied current. In this regime, flow rates have minimal influence on effluent stream profiles. Instead, the effluent concentration is determined by interplay among the cell volume (and associated initial amount of salt contained within the electrode), the rate at which diffusion and dispersion can supply new salt, and the applied current. In this regime, transport is limited by simple molecular diffusion. The appropriate time scale for normalization is $t_{diff} = L_e^2/D_{eff}$ and the appropriate concentration scale is the cell initial concentration c_0.

DOI: 10.1021/acs.jpcb.7b09168
J. Phys. Chem. B 2018, 122, 240−249

Figure 4 shows the normalized simulation results from area-averaged model and normalized experimental data in this regime.

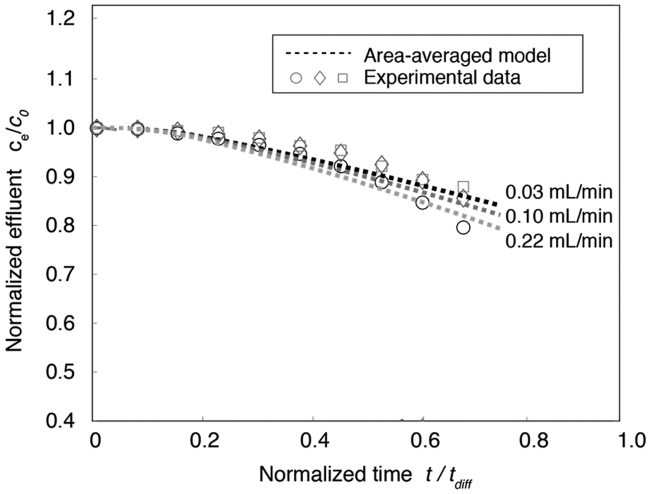

Figure 4. Effluent concentration profiles normalized by feed concentration c_0 from experiments (markers) and area-averaged model simulations (short-dotted grayscale lines) in dispersion-limited regime, with flow rates at 0.03, 0.10, and 0.22 mL/min. The fteCDI cell is operated in constant current charging mode at 50 mA. The area-averaged model successfully captures the magnitude and shape of the effluent concentration versus time.

We note that there is no quasi-steady state in the dispersion-limited region. As we explained above, the dispersion limited regime is associated with a globally starved cell wherein cell charging proceeds until the maximum allowable charging voltage is achieved. As shown in Figure 4, the area-averaged model successfully predicts the experimental effluent streams as data for all three flow rates clustered tightly along simulation results.

The dispersion-limited regime study helps to identify a limiting behavior of operational regimes in a CDI system and may also be useful in analyzing limiting behaviors of batch mode operation, wherein charging occurs at stopped flow conditions between intermittent flow operation.

CONCLUSIONS

We presented our studies on understanding and characterizing the coupling effects of charging and mass transport in flow-through electrode capacitive deionization systems. We developed two transport and electro-adsorption/desorption models. The first is an unsteady zero-dimensional volume-averaged model, and the second is a higher fidelity area-averaged model. The volume-averaged model applies to advection-limited transport regime and suggests key dimensionless parameters to characterize charging and mass transport. In this model, we also developed a formulation for lumped differential charge efficiency which conveniently describes electrical charge accumulation to salt removal using two explicit expressions (for early and later-stage charging). The higher fidelity area-averaged model is formulated in terms of average of the area perpendicular to the flow direction and captures both temporal and spatial responses of an fteCDI cell during charging process. The area-averaged model benchmarks the analytical model, confirms the utility of figures of merit of the volume-averaged model, and is also able to predict effluent concentration of an fteCDI in both advection-limited and dispersion-limited transport regimes.

In the advection-limited transport regime, flow rate, differential charge efficiency, and applied current determine the deionization dynamics of an fteCDI cell. The dimensionless parameters suggested by the volume-averaged model well collapse simulation results from both models. More importantly, these dimensionless parameters nicely collapse experimental data into a tight group. Our study also shows two important time regimes associated with differential charge efficiency. Early charging is characterized by a rise in differential charge efficiency from zero to unity over a time scale of the form $t_\lambda = 8p_M V_e c_0 F/I_0$. Subsequent charging benefits from unity differential charge efficiency. The charging state later results in a quasi-steady operation regime wherein near unity charge efficiency results in an inlet-to-outlet drop in salt concentration of the form $c_e - c_0 = I_0/(FQ)$ (directly proportional to a ratio of applied current I_0 and flow rate Q).

In the dispersion-limited regime, both differential charge efficiency and dispersion are critical for salt adsorption/desorption dynamics, whereas flow has negligible effect on deionization dynamics.

In both regimes, the interplay among differential charge efficiency, charging current, and mass transport rate governs salt removal in flow-through CDI. Our study provides guidance for designing and optimizing operation procedures to further improve desalination performance and water recovery for a variety of CDI systems.

ASSOCIATED CONTENT

Supporting Information

The Supporting Information is available free of charge on the ACS Publications website at DOI: 10.1021/acs.jpcb.7b09168.

Derivation of one-dimensional transport equation in macropores, expressions of salt adsorption and electrode surface charge density in Gouy−Chapman-Stern electrical double layer model, detailed derivation of zero-dimensional ODE for volume-averaged model, analytical solutions to ODEs of volume-averaged model, area-averaged model of flow-through electrode CDI system with constant voltage operation, fitting parameter extraction from near-equilibrium experiments, plot of cell potential over time during charging, and spatiotemporal plots of salt concentrations predicted by the area-averaged model. (PDF)

AUTHOR INFORMATION

Corresponding Authors

*E-mail: stadermann2@llnl.gov
*E-mail: juan.santiago@stanford.edu

ORCID

Yatian Qu: 0000-0001-8352-9492
Juan G. Santiago: 0000-0001-8652-5411

Notes

The authors declare no competing financial interest.

ACKNOWLEDGMENTS

Y.Q. would like to thank the Lawrence Scholar program. This work was supported by LLNL LDRD Project 15-ERD-068. Work at LLNL was performed under the auspices of the U.S. DOE by LLNL under Contract DE-AC52-07NA27344.

DOI: 10.1021/acs.jpcb.7b09168
J. Phys. Chem. B 2018, 122, 240−249

REFERENCES

(1) Suss, M. E.; Porada, S.; Sun, X.; Biesheuvel, P. M.; Yoon, J.; Presser, V. Water Desalination Via Capacitive Deionization: What Is It and What Can We Expect from It? *Energy Environ. Sci.* **2015**, *8*, 2296−2319.

(2) Porada, S.; Zhao, R.; van der Wal, A.; Presser, V.; Biesheuvel, P. M. Review on the Science and Technology of Water Desalination by Capacitive Deionization. *Prog. Mater. Sci.* **2013**, *58*, 1388−1442.

(3) Humplik, T.; Lee, J.; O'hern, S.; Fellman, B.; Baig, M.; Hassan, S.; Atieh, M.; Rahman, F.; Laoui, T.; Karnik, R.; Wang, E. N. Nanostructured Materials for Water Desalination. *Nanotechnology* **2011**, *22*, 292001.

(4) Zhao, R.; Biesheuvel, P. M.; van der Wal, A. Energy Consumption and Constant Current Operation in Membrane Capacitive Deionization. *Energy Environ. Sci.* **2012**, *5*, 9520.

(5) Biesheuvel, P. M.; van der Wal, A. Membrane Capacitive Deionization. *J. Membr. Sci.* **2010**, *346*, 256−262.

(6) Gao, X.; Omosebi, A.; Landon, J.; Liu, K. Surface Charge Enhanced Carbon Electrodes for Stable and Efficient Capacitive Deionization Using Inverted Adsorption−Desorption Behavior. *Energy Environ. Sci.* **2015**, *8*, 897−909.

(7) Bian, Y.; Yang, X.; Liang, P.; Jiang, Y.; Zhang, C.; Huang, X. Enhanced Desalination Performance of Membrane Capacitive Deionization Cells by Packing the Flow Chamber with Granular Activated Carbon. *Water Res.* **2015**, *85*, 371−376.

(8) Hemmatifar, A.; Palko, J. W.; Stadermann, M.; Santiago, J. G. Energy Breakdown in Capacitive Desalination. *Water Res.* **2016**, *104*, 303−311.

(9) Biesheuvel, P. M.; Limpt, B. v.; Wal, A. v. d. Dynamic Adsorption/Desorption Process Model for Capacitive Deionization. *J. Phys. Chem. C* **2009**, *113*, 5636−5640.

(10) Jande, Y. A. C.; Kim, W. S. Predicting the Lowest Effluent Concentration in Capacitive Deionization. *Sep. Purif. Technol.* **2013**, *115*, 224−230.

(11) Jande, Y. A. C.; Kim, W. S. Desalination Using Capacitive Deionization at Constant Current. *Desalination* **2013**, *329*, 29−34.

(12) Suss, M. E.; Baumann, T. F.; Bourcier, W. L.; Spadaccini, C. M.; Rose, K. A.; Santiago, J. G.; Stadermann, M. Capacitive Desalination with Flow-Through Electrodes. *Energy Environ. Sci.* **2012**, *5*, 9511.

(13) Qu, Y.; Baumann, T. F.; Santiago, J. G.; Stadermann, M. Characterization of Resistances of a Capacitive Deionization System. *Environ. Sci. Technol.* **2015**, *49*, 9699−9706.

(14) Qu, Y.; Campbell, P. G.; Gu, L.; Knipe, J. M.; Dzenitis, E.; Santiago, J. G.; Stadermann, M. Energy Consumption Analysis of Constant Voltage and Constant Current Operations in Capacitive Deionization. *Desalination* **2016**, *400*, 18−24.

(15) Johnson, A. M.; Venolia, A. W.; Newman, J.; Wilbourne, R. G.; Wong, C. M.; Gilliam, W. S.; Johnson, S.; Horowitz, R. H. *The Electrosorb Process for Desalting Water*; United States Department of the Interior: Washington, DC, 1970.

(16) Bouhadana, Y.; Avraham, E.; Noked, M.; Ben-Tzion, M.; Soffer, A.; Aurbach, D. Capacitive Deionization of Nacl Solutions at Non-Steady-State Conditions: Inversion Functionality of the Carbon Electrodes. *J. Phys. Chem. C* **2011**, *115*, 16567−16573.

(17) Guyes, E. N.; Shocron, A. N.; Simanovski, A.; Biesheuvel, P.; Suss, M. E. A One-Dimensional Model for Water Desalination by Flow-through Electrode Capacitive Deionization. *Desalination* **2017**, *415*, 8−13.

(18) Biesheuvel, P. M.; Fu, Y.; Bazant, M. Z. Diffuse Charge and Faradaic Reactions in Porous Electrodes. *Phys. Rev. E: Stat., Nonlinear, Soft Matter Phys.* **2011**, *83*, 061507.

(19) Hemmatifar, A.; Stadermann, M.; Santiago, J. G. Two-Dimensional Porous Electrode Model for Capacitive Deionization. *J. Phys. Chem. C* **2015**, *119* (44), 24681−24694.

(20) Suss, M. E.; Biesheuvel, P. M.; Baumann, T. F.; Stadermann, M.; Santiago, J. G. In Situ Spatially and Temporally Resolved Measurements of Salt Concentration between Charging Porous Electrodes for Desalination by Capacitive Deionization. *Environ. Sci. Technol.* **2014**, *48*, 2008−2015.

(21) Tang, W.; Kovalsky, P.; Cao, B.; Waite, T. D. Investigation of Fluoride Removal from Low-Salinity Groundwater by Single-Pass Constant-Voltage Capacitive Deionization. *Water Res.* **2016**, *99*, 112−121.

(22) Biesheuvel, P. M.; Hamelers, H. V. M; Suss, M. E. Theory of Water Desalination by Porous Electrodes with Immobile Chemical Charge. *Colloids Interface Sci. Commun.* **2015**, *9*, 1−5.

(23) Gao, X.; Omosebi, A.; Landon, J.; Liu, K. Enhanced Salt Removal in an Inverted Capacitive Deionization Cell Using Amine Modified Microporous Carbon Cathodes. *Environ. Sci. Technol.* **2015**, *49*, 10920−10926.

(24) Gao, X.; Porada, S.; Omosebi, A.; Liu, K. L.; Biesheuvel, P. M.; Landon, J. Complementary Surface Charge for Enhanced Capacitive Deionization. *Water Res.* **2016**, *92*, 275−282.

(25) Baumann, T. F.; Worsley, M. A.; Han, T. Y.-J.; Satcher, J. H. High Surface Area Carbon Aerogel Monoliths with Hierarchical Porosity. *J. Non-Cryst. Solids* **2008**, *354*, 3513−3515.

(26) Biener, J.; Stadermann, M.; Suss, M.; Worsley, M. A.; Biener, M. M.; Rose, K. A.; Baumann, T. F. Advanced Carbon Aerogels for Energy Applications. *Energy Environ. Sci.* **2011**, *4*, 656.

(27) Newman, J.; Tiedemann, W. Desalting by Means of Porous Carbon Electrodes. *AIChE J.* **1975**, *21*, 25−41.

(28) Newman, J. S.; Tobias, C. W. Theoretical Analysis of Current Distribution in Porous Electrodes. *J. Electrochem. Soc.* **1962**, *109*, 1183−1191.

(29) Trainham, J. A.; Newman, J. A Flow-through Porous Electrode Model: Application to Metal-Ion Removal from Dilute Streams. *J. Electrochem. Soc.* **1977**, *124*, 1528−1540.

(30) Stern, H. O. Zur Theorie Der Elektrolytischen Doppelschicht. *Elektrochem.* **1924**, *30*, 508.

(31) Bazant, M. Z.; Thornton, K.; Ajdari, A. Diffuse-Charge Dynamics in Electrochemical Systems. *Phys. Rev. E* **2004**, *70*, 021506.

(32) Persat, A.; Santiago, J. G. An Ohmic Model for Electrokinetic Flows of Binary Asymmetric Electrolytes. *Curr. Opin. Colloid Interface Sci.* **2016**, *24*, 52−63.

(33) Burnett, R.; Frind, E. Simulation of Contaminant Transport in Three Dimensions: 2. Dimensionality Effects. *Water Resour. Res.* **1987**, *23*, 695−705.

(34) Lichtner, P. C.; Kelkar, S.; Robinson, B. A. *Critique of Burnett-Frind Dispersion Tensor for Axisymmetric Porous Media*; Los Alamos National Laboratory (LANL): Los Alamos, NM, 2008.

(35) Biesheuvel, P. M.; Zhao, R.; Porada, S.; van der Wal, A. Theory of Membrane Capacitive Deionization Including the Effect of the Electrode Pore Space. *J. Colloid Interface Sci.* **2011**, *360*, 239−248.

(36) Biesheuvel, P. M. *Activated Carbon Is an Electron-Conducting Amphoteric Ion Adsorbent* **2015**, *arXiv*, 1509−06354.

(37) Gao, X.; Omosebi, A.; Landon, J.; Liu, K. Dependence of the Capacitive Deionization Performance on Potential of Zero Charge Shifting of Carbon Xerogel Electrodes During Long-Term Operation. *J. Electrochem. Soc.* **2014**, *161*, E159−E166.

(38) Cohen, I.; Avraham, E.; Bouhadana, Y.; Soffer, A.; Aurbach, D. The Effect of the Flow-Regime, Reversal of Polarization, and Oxygen on the Long Term Stability in Capacitive De-Ionization Processes. *Electrochim. Acta* **2015**, *153*, 106−114.

(39) Bouhadana, Y.; Ben-Tzion, M.; Soffer, A.; Aurbach, D. A Control System for Operating and Investigating Reactors: The Demonstration of Parasitic Reactions in the Water Desalination by Capacitive De-Ionization. *Desalination* **2011**, *268*, 253−261.

(40) Lee, J.-H.; Bae, W.-S.; Choi, J.-H. Electrode Reactions and Adsorption/Desorption Performance Related to the Applied Potential in a Capacitive Deionization Process. *Desalination* **2010**, *258*, 159−163.

(41) He, D.; Wong, C. E.; Tang, W.; Kovalsky, P.; Waite, T. D. Faradaic Reactions in Water Desalination by Batch-Mode Capacitive Deionization. *Environ. Sci. Technol. Lett.* **2016**, *3*, 222−226.

(42) Kim, T.; Dykstra, J. E.; Porada, S.; van der Wal, A.; Yoon, J.; Biesheuvel, P. M. Enhanced Charge Efficiency and Reduced Energy Use in Capacitive Deionization by Increasing the Discharge Voltage. *J. Colloid Interface Sci.* **2015**, *446*, 317−326.

DOI: 10.1021/acs.jpcb.7b09168
J. Phys. Chem. B 2018, 122, 240−249